Metallography, Microstructure, and Analysis (2025) 14:106–119
https://doi.org/10.1007/s13632-025-01170-w

ORIGINAL RESEARCH ARTICLE

Comparison of Constituent Intermetallic Particles in Different Aluminium Alloys

João Victor de Sousa Araujo[1] · Isolda Costa[1] · Xiaorong Zhou[2]

Received: 29 August 2024 / Revised: 30 December 2024 / Accepted: 12 January 2025 / Published online: 24 January 2025

Abstract
This study quantitatively evaluates the variation in the distribution, density, size, and chemical composition of constituent intermetallic particles (IMPs) in different commercial high strength aluminium alloys, including Al-Cu-Mg (AA2024-T3), Al-Cu-Li (AA2198-T8/T851), and Al-Mg-Zn (AA7475-T761) alloys. It is observed that the AA2024-T3 alloy is characterized by three primary types of IMPs (Al-Cu-Mg, Al-Cu-Fe-Mn, and Al-Cu-Fe-Mn-Si) and the highest particle population density. In contrast, the Al-Cu-Li alloys contain a single type of IMP (Al-Cu-Fe), while the AA7475-T761 alloy exhibits the lowest population density of IMPs that are distinguished by varying copper contents.

Keywords Aluminium alloys · Microstructure characterization · Electron microscopy · Constituent intermetallic particles

Introduction

Constituent intermetallic particles (IMPs) are typically formed in aluminium (Al) alloys during the casting process due to the low solubility of alloying elements or impurities from bauxite ore extraction process or alloy recycling, such as Fe and Si [1–3]. Economically unfeasible or impossible to be removed from the alloys, these particles become inherent constituents of Al alloys [1, 4, 5]. IMPs are found in most aluminium alloy classes and are particularly notable in high strength alloys [6].

These particles influence critical aspects of the alloys, such as corrosion properties [7], fatigue durability [8], and anodization behaviour [9]. Their presence can lead to localized corrosion, reduction in mechanical properties, and variations in the quality of the anodized layer [10–12]. Therefore, an in-depth understanding of the distribution, density, size, and chemical composition of these particles is essential for the development and optimization of high-performance aluminium alloys.

Over the decades, various researchers [13–24] have studied the electrochemical and corrosion properties of IMPs in aluminium alloys. It was found that the composition of these particles determines their cathodic or anodic nature relative to alloy matrix when subjected to a corrosive environment, which often results in a reduction in corrosion resistance [25]. Further, in the context of anodization that is widely used in industry for forming corrosion protective anodic film on aluminium alloys for engineering applications, the designation of anodic and cathodic nature of IMPs is inadequate since during the anodic oxidation process, aluminium alloy, including alloy matrix and IMPs, is subjected to an anodic polarization. However, in terms of anodic oxidation behaviour, the classification of the IMPs is based on their oxidation/dissolution rate relative to Al matrix [26–28]. The dissolution of these particles can lead to the formation of defects and discontinuities in the resultant anodic films [29]. Therefore, understanding the chemical composition, morphology, and distribution of these particles in Al alloys is crucial for the optimization of anodization.

While significant research has been conducted on individual aluminium alloys [13–15, 23, 30–39], there is need to better understand on how variations in IMPs characteristics across different alloy systems influence their electrochemical and corrosion properties. This is especially true concerning the anodizing behaviour and the corrosion properties of anodized aluminium alloys since the same anodizing process is normally applied to different alloy systems in industry.

✉ João Victor de Sousa Araujo
jvaraujo@usp.br

[1] Centro de Ciência e Tecnologia de Materiais, Instituto de Pesquisas Energéticas e Nucleares–IPEN/CNEN–Av. Prof. Prof. Lineu Prestes, São Paulo 2242, Brasil

[2] Corrosion and Protection Centre, Department of Materials, The University of Manchester, Manchester M13 9PL, UK

The characteristics of IMPs inevitably introduce local variation in anodic film composition and morphology associated with the anodic oxidation behaviour of the individual particles. Although standard handbooks of physical metallurgy provide foundational knowledge on aluminium alloys, they often lack detailed discussions on how IMPs characteristics vary between different alloy systems and how these variations impact critical properties such as corrosion resistance and anodizing behaviour [40, 41]. This gap highlights the need for comparative studies like the present one, which explores IMPs characteristics in specific alloy families and their practical implications.

This paper aims to address a specific question, that is: What are the main differences between constituent intermetallic particles present in Al-Cu-Mg, Al-Cu-Li, and Al-Zn-Mg alloys, especially their distribution, density, size, and chemical composition?

Experimental

This study examines the microstructural characterization of four commercial aluminium alloys—AA2024-T3 (Al–Cu–Mg), AA2198-T8 and AA2198-T851 (Al–Cu–Li), and AA7475-T761 (Al–Zn–Mg)—all supplied as rolled sheets. The elemental composition, determined by ICP-OES, is detailed in Table 1. The alloys were analysed in their commercial temper conditions: T3 for AA2024 (solution heat treated, cold worked, naturally aged), T8 and T851 for AA2198 (solution heat treated, cold worked, artificially aged; T851 includes additional stretching), and T761 for AA7475 (solution heat treated, cold worked, stress relieved, artificially aged) [42].

Specimen Preparation

The surface of the alloys was mechanically ground using silicon carbide sandpaper with sequentially grit sizes P800, P1200, P2400, and P4000, followed by sequential polishing with 3 µm and 1 µm diamond paste. After mechanical polishing, the specimens were degreased in acetone, rinsed in deionized water, and dried using a cold air jet.

Microstructural Characterization

Scanning Electron Microscopy (SEM)

For a thorough analysis of the morphology and composition of areas of interest on the surfaces of the alloys, before the procedure described in (a), the Quanta^{TM} 650 FEG microscope was used, coupled with energy-dispersive X-ray spectroscopy (EDX). Images and EDX analyses were obtained using an acceleration voltage of 20 kV.

Scanning Kelvin Probe Force Microscopy (SKPFM)

Scanning Kelvin Probe Force Microscopy (SKPFM) was performed using the Nanoscope IIIa MultiMode microscope in tapping mode. To SKPFM analyses, both, topographic and surface potential images, were captured using the lift mode. The measurements were carried out at room temperature and humidity levels ranging from 30 to 55%. The collected data were analysed using NanoScope Analyses 1.5 software.

Table 1 Chemical composition of the studied alloys (wt.%) obtained by inductively coupled plasma optical emission spectrometry (ICP-OES)

Elements	Aluminium alloys			
	AA2024-T3	AA2198-T8	AA2198-T851	AA7475-T761
Al	*Balance*			
Cu	4.8 (3.8–4.9)	3.34 (2.9–3.5)	3.31 (2.9–3.5)	1.52 (1.2–1.9)
Mg	0.59 (1.2–1.8)	0.31 (0.25–0.80)	0.31 (0.25–0.80)	1.8 (1.9–2.6)
Mn	0.52 (0.3–0.9)	0.003 (≤ 0.50)	0.003 (≤ 0.50)	0.05 (≤ 0.06)
Li	–	0.95 (0.81–1.1)	0.96 (0.81–1.1)	–
Fe	0.18 (≤ 0.5)	0.04 (≤ 0.10)	0.04 (≤ 0.10)	0.07 (≤ 0.12)
Zn	0.11 (≤ 0.25)	0.006 (≤ 0.35)	0.006 (≤ 0.35)	6.10 (5.2–6.2)
Si	0.07 (≤ 0.5)	0.04 (≤ 0.08)	0.03 (≤ 0.08)	0.03 (≤ 0.06)
Zr	–	0.05 (0.04–0.18)	0.05 (0.04–0.18)	–
Ag	–	0.26 (0.2–0.3)	0.25 (0.2–0.3)	–
Cr	–	–		0.20 (0.18–0.25)

Values in parentheses present the composition specification according to ASM [43] for the aluminium alloys.

Image Analyser to Microstructural Characterization

Statistical analysis of each alloy was carried out using ImageJ® software, enabling the examination of IMPs characteristics, such as size, distribution, and density.

Results

Figure 1 presents scanning electron micrographs of the surfaces of the four studied aluminium alloys, emphasizing the distribution of IMPs.

The AA2024-T3 alloy (Fig. 1a1–a3) shows a relatively uniform distribution of IMPs at low magnification (Fig. 1a1), which becomes more discernible and aligned along the rolling direction (indicated by yellow arrows) at higher magnification (Fig. 1a3). The AA2198-T8 alloy (Fig. 1b1-b3) exhibits a slightly more dispersed particle distribution at low magnification (Fig. 1b1), with clear alignment at the highest magnification (Fig. 1b3). The AA2198-T851 alloy (Fig. 1c1–c3) has a significant amount of IMPs, less dense than the AA2024-T3, but more uniformly distributed, as it shows at low magnification (Fig. 1c1) with evident alignment at higher magnification (Figure 1c3). The AA7475-T761 alloy (Fig. 1d1–d3) shows fewer and more spaced particles than the other studied alloys, as it shows at low magnification (Fig. 1d1), with a less pronounced alignment at higher magnification (Fig. 1d3), indicating a reduced influence of mechanical processing. This detailed multi-scale analysis highlights the intrinsic differences in particle distribution and alignment among the 2XXX and 7XXX aluminium alloys, which are crucial for understanding their performance in aerospace applications. This detailed multi-scale analysis reveals differences in particle distribution and alignment within the studied batches of 2XXX and 7XXX aluminium alloys. However, these characteristics are not inherently characteristic of all alloys within these series, as they are closely linked to the specific fabrication processes and parameters used in each batch. Thus, the findings underscore the critical role of fabrication history in assessing the performance of these alloys, particularly in aerospace applications. Although these particles do not contribute to increase mechanical strength, they significantly influence the corrosion development process [5] and anodizing behaviour [9].

The distribution of IMPs in both alloys is shown in Fig. 2, as presented by the histograms. The plots represent particle counts as a function of size (µm), highlighting the variability in the distribution and size of IMPs between different alloys. In the SEM images, blue circles and yellow circles represent particles larger and smaller than 5 µm, respectively.

In the AA2024-T3 alloy (Fig. 2a), there is a predominance of small particles, mainly below 5 µm, with some larger particles reaching up to 20 µm. SEM images (Fig 2a1) confirm this distribution, showing a dense concentration of small particles (yellow circles) with a few larger particles (blue circles). The AA2198-T8 alloy (Fig. 2b) shows a similar trend, with a concentration of smaller particles but a broader distribution, compared to the AA2024-T3. SEM images (Fig. 2b1) illustrate this distribution, with a variety of particle sizes scattered across the surface. In the AA2198-T851 alloy (Fig. 2c), particle distribution is narrower, with most particles size below 10 µm. SEM images (Fig. 2c1) support this observation, showing fewer large particles and a more uniform distribution of smaller particles. Finally, the AA7475-T761 alloy (Fig. 2d) reveals the lowest density of

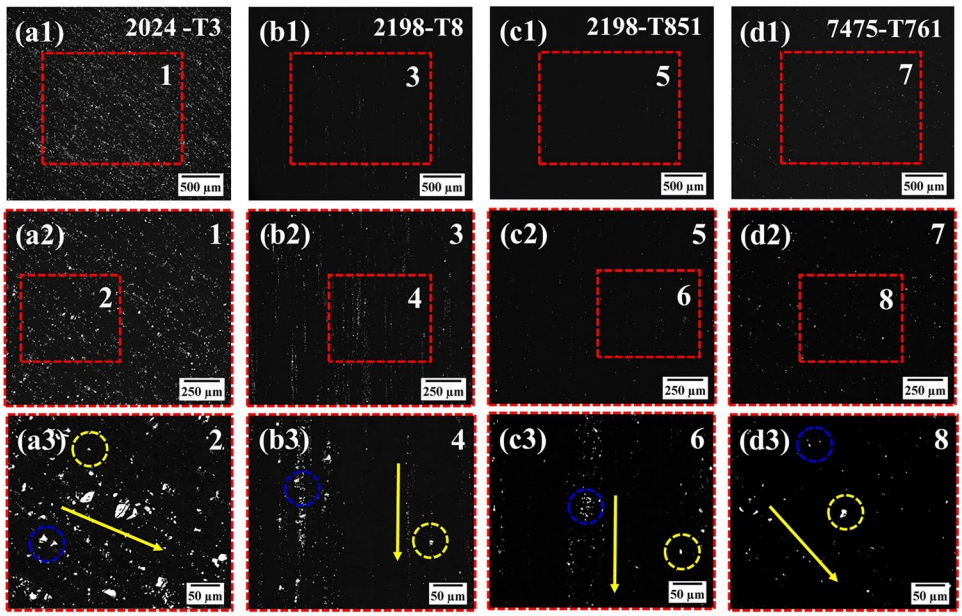

Fig. 1 Scanning electron micrographs of the tested aluminium alloys, showing constituent intermetallic particles (IMPs): **a1**, **b1**, **c1**, and **d1** at low magnification; higher magnification **a2**, **b2**, **c2**, and **d2** of the dashed regions in (**a1**, **b1**, **c1**, and **d1**); and **a3**, **b3**, **c3**, and **d3** higher magnification of the dashed regions in (**a2**, **b2**, **c2**, and **d2**). The yellow arrows indicate the rolling direction. The yellow and blue circles indicate isolated and clustered particles in (**a3–d3**), respectively

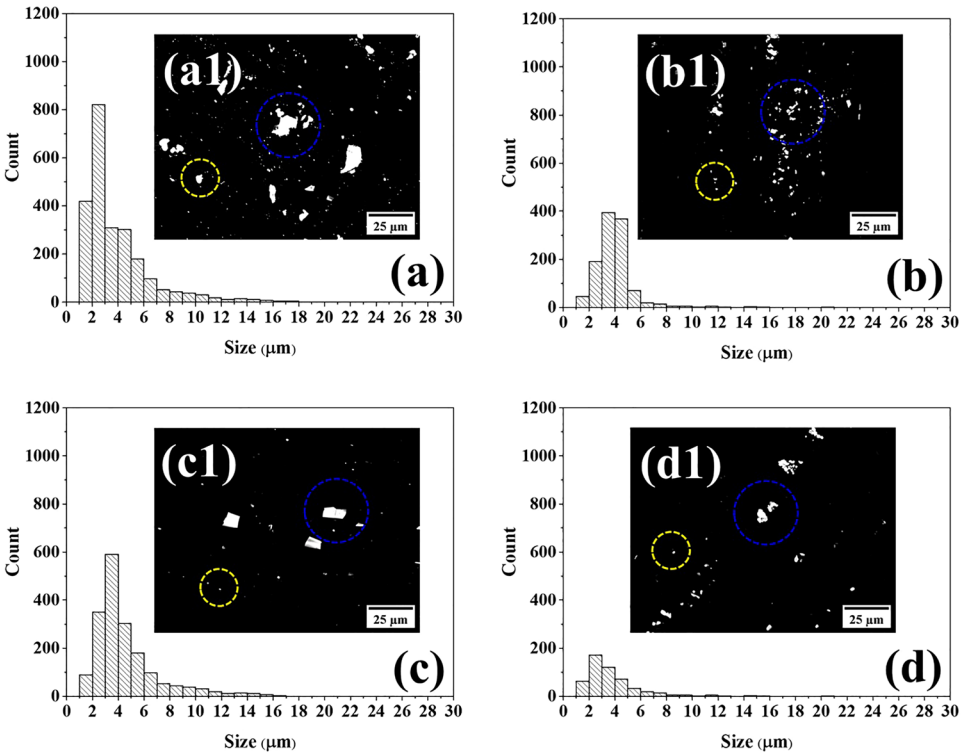

Fig. 2 Histograms **a**–**d** and scanning electron microscopy (SEM) images **a1**–**d1** of AA2024-T3, AA2198-T8, AA2198-T851, and AA7475-T761 alloys, showing the distribution of IMPs. The histograms represent the particle count as a function of size (μm), highlighting the variability in the distribution and size of IMPs among different alloys. Yellow and blue circles in the SEM images represent particles larger and smaller than 5 μm, respectively

IMPs, with smaller than 5 μm. SEM images (Fig. 2d1) show a sparse distribution of particles, with fewer occurrences of larger particles.

Following the detailed microstructural analysis presented in Figs 1 and 2, Table provides statistical data of the IMPs in the studied aluminium alloys.

Table 2 shows that the AA2024-T3 alloy has the highest population density of IMPs ($3472 \pm 157/mm^2$) with the second largest average size (3.9 ± 2.6 μm) and the highest percentage area covered by these particles (1.4%). In contrast, the AA7475-T761 alloy has the lowest population density ($626 \pm 75/mm^2$), with the smallest average size (3.7 ± 2.1 μm) and the lowest percentage area (0.14%). The AA2198-T8 and AA2198-T851 alloys have intermediate values, with the T8 alloy showing a higher population density ($1948 \pm 242/mm^2$) compared to the T851 one ($1389 \pm 149/mm^2$), but both alloys have similar percentage areas (0.25% for T8 and 0.22% for T851). Regarding average particle size, the AA2198-T8 alloy (4.6 ± 2.5 μm) has the largest particles among the alloys studied, while the T851 condition (3.8 ± 1.5 μm) has values closer to those of the AA2024-T3.

To better highlight these variations, the relative differences in population density and average particle size were calculated using the AA2024-T3 alloy as a reference. The results show that the population density in the AA2198-T8 and AA7475-T761 alloys is 44% and 82% lower, respectively, compared to the AA2024-T3 alloy. Similarly, the AA2198-T851 alloy has a 60% lower population density than the reference alloy. In terms of average particle size, the AA2198-T8 alloy displays an 18% increase relative to the AA2024-T3 alloy, while the AA2198-T851 alloy shows a slightly smaller size difference of −3%. The AA7475-T761

Table 2 Statistical data of the constituent intermetallic particles (IMPs) present in the alloys used in this study. Results obtained through the analysis of 20 randomly selected areas, each with dimensions of 3 × 2.5 mm

Aluminium alloy	Density (particles/mm^2)	Relative difference (%)	Average size (μm)	Relative difference (%)	Area (%)
AA2024-T3	3472 ± 157	–	3.9 ± 2.6	–	1.4
AA2198-T8	1948 ± 242	−44	4.6 ± 2.5	+18	0.25
AA2198-T851	1389 ± 149	−60	3.8 ± 1.5	−3	0.22
AA7475-T761	626 ± 75	−82	3.7 ± 2.1	−5	0.14

The relative difference is calculated using AA2024-T3 as the reference alloy.

alloy has the smallest average particle size, with a relative difference of − 5% compared to the reference alloy (AA2024-T3).

These relative differences underline the impact of chemical composition and thermomechanical treatments on the microstructure of the alloys. The higher population density observed in the AA2024-T3 alloy reflects its higher content of Cu and Fe, which promotes the formation of intermetallic phases. Conversely, the lower density in the AA7475-T761 alloy can be attributed to the predominance of Zn and Mg, which exhibit higher solubility in the aluminium matrix and therefore result in fewer intermetallic particles. The larger average size of particles in the AA2198-T8 alloy may be a consequence of the presence of Li, which modifies the precipitation dynamics of intermetallic phases. Similarly, the intermediate behaviour observed in the AA2198-T851 alloy suggests that its thermomechanical treatment reduces the formation of large intermetallic particles, yielding characteristics closer to those of the AA2024-T3 alloy.

The high particle density in the AA2024-T3 alloy, combined with its greater compositional complexity, is associated with increased susceptibility to localized corrosion. On the other hand, the lower density in the AA7475-T761 suggests greater resistance in corrosive environments, highlighting the suitability of this alloy for aerospace applications.

The distribution of elements in the IMPs was initially analysed using energy-dispersive X-ray spectroscopy (EDX) mapping, as presented in Fig. 3. Figure 3a–e shows scanning electron micrographs of the aluminium alloy surfaces, highlighting the IMPs, while Fig. 3a1–e1 presents the corresponding EDX maps.

In the AA2024-T3 alloy (Fig. 3a–b1), two types of IMPs were identified. One contains significant amounts of aluminium (Al), copper (Cu), and magnesium (Mg) (Fig. 3a1), while the other includes additional elements such as iron (Fe), manganese (Mn), and silicon (Si) (Fig. 3b1).

The AA2198 alloy in both treatments, T8 and T851 (Fig. 3c–d1), exhibits similar intermetallic particle compositions. The EDX maps show the presence of Al, Cu, and Fe within these particles. In an initial analysis, the AA7475-T761 alloy (Fig. 3e and e1) shows a distribution of elements like that of the AA2198 tested alloys. This suggests that although the overall chemical composition of the alloys differs, the composition of the IMPs is similar.

EDX maps (Fig. 3) reveal the spatial distribution of elements across alloy surfaces; spot EDX analysis allows precise measurement of elemental concentrations at specific locations within IMPs. This provides a more accurate understanding of the composition of individual particles and facilitates deeper insight into variations in elemental content, as shown in Fig. 4.

In the AA2024-T3 alloy (Fig. 4a), three types of IMPs are evident. Particle 1 is composed of Al (63.3 wt.%), Cu (23.5 wt.%), and Mg (13.2 wt.%); particle 2 contains Al (72.1 wt.%), Cu (12.5 wt.%), Fe (9.1 wt.%), and Mn (5.4 wt.%); and particle 3 consists of Al (71.1 wt.%), Cu (12.5 wt.%), Fe (9.1 wt.%), Mn (4.2 wt.%), and Si (3.1 wt.%). The EDX spectra in Fig. 4 highlight the variability in the composition of IMPs within the AA2024-T3 alloy. As indicated in Table 3, the analysis of 60 individual particles from this alloy shows distinct variations in Cu, Mg, Mn, and Si content, with average compositions of Al-Cu-Mg (Al 58.2% ± 11.2%, Cu 27.2% ± 11.1%, Mg 14.6% ± 5.1%), Al-Cu-Fe-Mn (Al 75.2% ± 8.9%, Cu 15.6% ± 3.6%, Fe 5.4% ± 2.4%, Mn 3.8% ± 1.2%), and Al-Cu-Fe-Mn-Si (Al 60.4% ± 5%, Cu 18.5% ± 3.1%, Fe 12% ± 1.8%, Mn 6.9% ± 1.3%, Si 2.2% ± 1.1%).

For the AA2198-T8 alloy (Fig. 4b), an intermetallic particle (particle 4) is composed of Al (61.5 wt.%), Cu (25.4 wt.%), and Fe (13.1 wt.%). Similarly, the AA2198-T851 alloy (Fig. 4c) reveals an intermetallic particle (particle 5) with Al (63.3 wt.%), Cu (26.1 wt.%), and Fe (10.6 wt.%). The EDX spectra (Fig. 4c1) show similar compositions to the AA2198-T8 alloy, with slight variations in the Cu and Fe content. Table 3 further supports these findings, indicating an average composition for AA2198-T8 of Al (61.7% ± 9.6%), Cu (27.9% ± 7.1%), Fe (10.1% ± 2.7%), and for AA2198-T851 of Al (50.1% ± 8.8%), Cu (38.5% ± 7.6%), Fe (11.1% ± 3.2%).

Although the EDX analysis employed in this study was unable to detect lithium in the intermetallic particles of the AA2198-T8 and AA2198-T851 alloys, it is important to consider the lithium content in the alloys, approximately 1 wt.%. Previous studies on similar Al-Cu-Li alloys have suggested that particles with high copper content likely contain significant amounts of lithium, which remains undetectable by conventional EDX methods due to its low atomic number [44]. This suggestion was later confirmed through more suitable techniques, such as electron microprobe analysis equipped with a soft X-ray emission spectrometer (SXES) [45], which revealed the presence of lithium in the intermetallic particles of Al-Cu-Li alloys. Thus, it is possible that the intermetallic particles identified in the present study also contain lithium, even though this was not detectable with the analytical techniques employed.

In the AA7475-T761 alloy (Fig. 4d), two types of IMPs are observed: particle 6 contains Al (77.3 wt.%), Cu (6.1 wt.%), and Fe (16.6 wt.%), while particle 7 is composed of Al (63.3 wt.%), Cu (26.1 wt.%), and Fe (10.6 wt.%). The EDX spectra (Fig. 4d1) highlight the varying copper content in these particles, with spectrum 6 showing lower levels of Cu and spectrum 7 showing higher levels of Cu. Table 3 corroborates this, indicating that high-copper-content particles have an average composition of Al (57.3% ± 9.3%), Cu (27.5% ± 2.6%), and Fe (15.2% ± 4.4%),

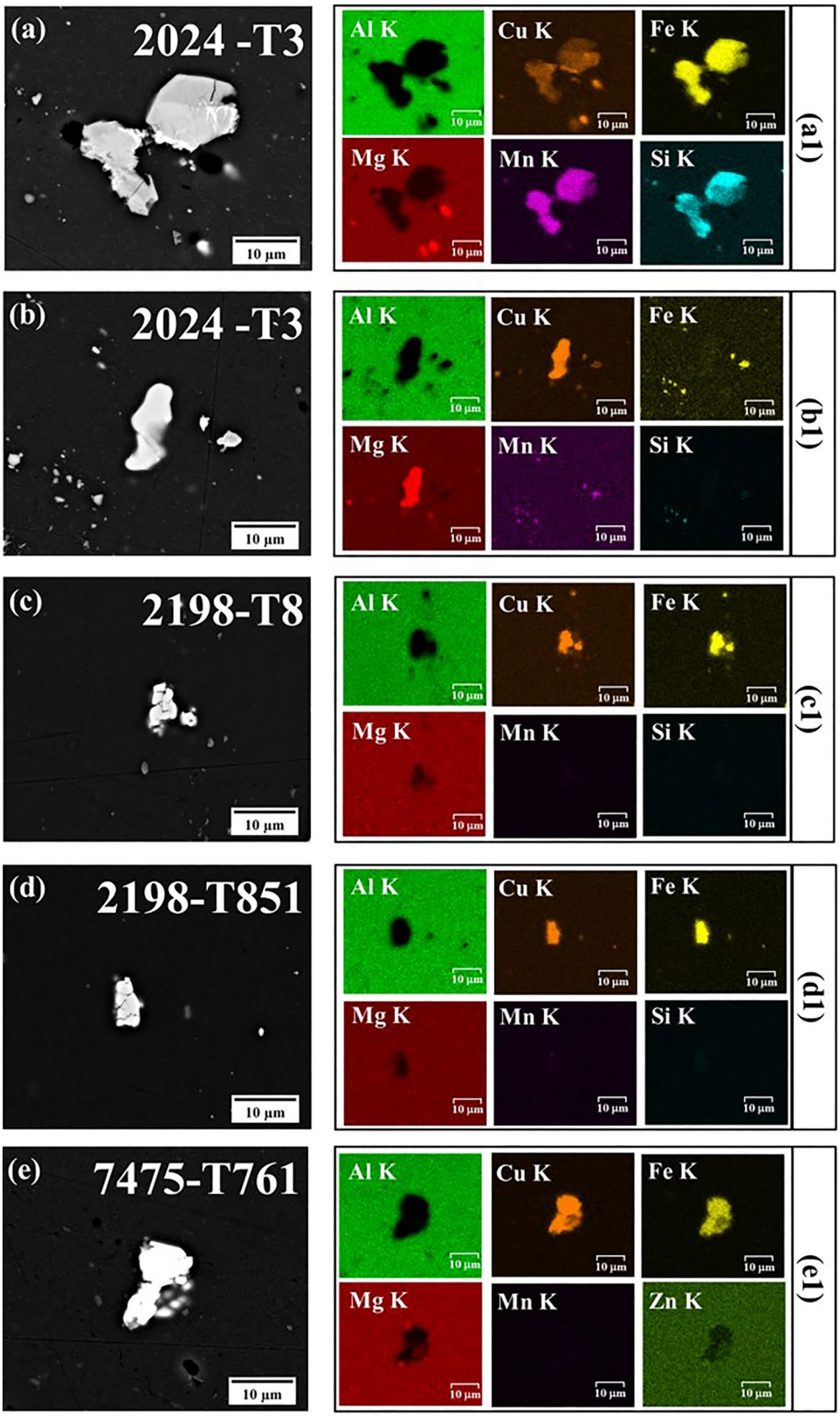

Fig. 3 Scanning electron micrographs of the Al alloys surface showing **a**–**e** constituent intermetallic particles (IMPs) and corresponding EDX elemental maps (**a1**–**e1**) illustrating the distribution of elements within the IMPs

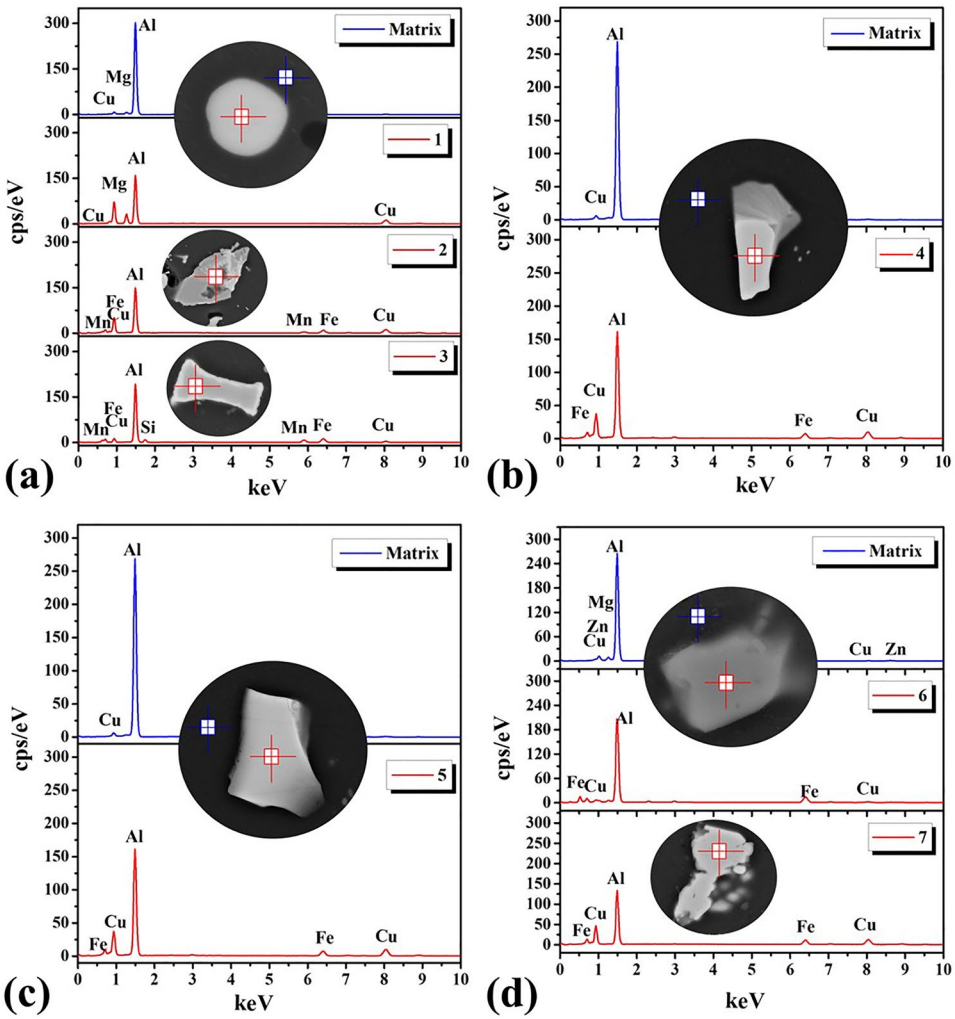

Fig. 4 **a**–**d** Scanning electron micrographs of the Al alloy surface showing constituent intermetallic particles (IMPs) and their corresponding EDX spectra, taken from red points (IMPs) and blue points (alloy matrix) as indicated in (**a**–**d**)

Table 3 Average composition of the constituent intermetallic particles (IMPs) present in the Al alloys used in this study (wt.%). Results obtained through the analysis of 60 IMPs in each alloy

Aluminium alloys	EDX point	Al	Cu	Fe	Mg	Mn	Si	Zn
AA2024-T3	Al-Matrix	95.1 ± 2.3	3.8 ± 1.4	–	1.1 ± 1.0	–	–	–
	Al-Cu-Mg	58.2 ± 11.2	27.2 ± 11.1	–	14.6 ± 5.1	–	–	–
	Al-Cu-Fe-Mn	75.2 ± 8.9	15.6 ± 3.6	5.4 ± 2.4	–	3.8 ± 1.2	-	-
	Al-Cu-Fe-Mn-Si	60.4 ± 5	18.5 ± 3.1	12 ± 1.8	–	6.9 ± 1.3	2.2 ± 1.1	-
AA2198-T8	Al-Matrix	95.8 ± 0.8	3.9 ± 0.8	–	0.3 ± 0.1	–	–	–
	Al-Cu-Fe	61.7 ± 9.6	27.9 ± 7.1	10.1 ± 2.7	–	–	–	–
AA2198-T851	Al-Matrix	94.2 ± 0.3	5.5 ± 0.3	-	0.3 ± 0.1	–	–	–
	Al-Cu-Fe	50.1 ± 8.8	38.5 ± 7.6	11.1 ± 3.2	–	–	–	–
AA7475-T761	Al-Matrix	90.2 ± 1.9	1.7 ± 0.8	–	2.3 ± 0.08	-	-	5.8 ± 0.2
	Al-Cu-Fe (High-copper- containing)	57.3 ± 9.3	27.5 ± 2.6	15.2 ± 4.4	–	–	–	–
	Al-Cu-Fe (Low-copper- containing)	78.5 ± 7.59	5.4 ± 1.5	16.1 ± 6.6	–	–	–	–

* Lithium cannot be detected by the EDX employed in the present work.

while low-copper-content particles have an average composition of Al (78.5% ± 7.59%), Cu (5.4% ± 1.5%), and Fe (16.1% ± 6.6%).

These findings emphasize the significant compositional differences and similarities among the alloys, particularly in terms of Cu, Mg, Mn, and Si for AA2024-T3; Cu and Fe for AA2198; and copper content for AA7475-T761.

The analysis of IMPs in these alloys provides a deeper understanding of the compositional differences that can influence their properties and performance. To further quantify these differences, the average Cu/Fe and Cu/Mg ratios of the IMPs present in the aluminium alloys studied are presented in Table 4.

Table 4 presents the average Cu/Fe and Cu/Mg ratios of the IMPs present in the aluminium alloys used in this study, with the results obtained through the analysis of 60 IMPs in each alloy. For the AA2024-T3 alloy, the Al-Cu-Mg particles exhibit a Cu/Mg ratio of (2.20 ± 0.9), while the Al-Cu-Fe-Mn particles show a Cu/Fe ratio of (3.1 ± 0.6), and the Al-Cu-Fe-Mn-Si particles have a Cu/Fe ratio of (1.5 ± 0.2). The AA2198-T8 alloy has a Cu/Fe ratio of (2.8 ± 0.4) for its IMPs. Similarly, the AA2198-T851 alloy displays a Cu/Fe ratio of (2.6 ± 0.2). In the AA7475-T761 alloy, the high Cu IMPs have a Cu/Fe ratio of (2.16 ± 0.3), and the low Cu particles exhibit a Cu/Fe ratio of (0.4 ± 0.1).

The similarities in the Cu/Fe ratios for the AA2198 alloys reinforce that the composition of the IMPs in these alloys is comparable. In contrast, the AA7475-T761 alloy shows significant differences in Cu/Fe ratios between high- and low-copper-containing IMPs, indicating a variation in IMPs composition. Additionally, the AA2024-T3 alloy exhibits distinct variations in the Cu/Fe ratios among its different types of IMPs, further highlighting the diverse composition of IMPs in this alloy.

Although the differences in Cu/Fe and Cu/Mg ratios may appear minor and within the margin of error of the EDX technique, they provide valuable insights into the compositional variability of the IMPs across the alloys studied. These differences, even when subtle, can significantly influence the electrochemical behaviour of the particles [18]. Higher Cu/Fe ratios, as observed in the AA2024-T3 alloy (3.1 ± 0.6), are associated with increased cathodic activity of intermetallic particles relative to the matrix [46]. This behaviour is known to promote trenching corrosion, where the localized cathodic activity around copper-rich IMPs accelerates the anodic dissolution of the surrounding matrix [47]. The lower Cu/Fe ratio observed in the AA7475-T761 alloy (2.16 ± 0.3), combined with the presence of low-copper-containing (Cu/Fe = 0.4 ± 0.1), suggests reduced cathodic activity of its IMPs, which likely contributes to its superior resistance to trenching corrosion compared to AA2024-T3.

The variations in the chemical composition of the particles in different alloys, as presented in the previous results, lead to differences in their potential relative to the matrix. This phenomenon is demonstrated in Fig. 5 through SKPFM analysis.

Although SKPFM cannot distinguish the exact chemical composition of the particles, the potential variation presented in (Fig. 5b) clearly shows a distinction between the IMPs and the aluminium matrix, consistent with findings reported in the literature [48]. Specifically, Fig. 5a presents AFM images of the IMPs and the surface potential map of these particles. Additionally, Fig. 5b shows a topography (blue line) and Volta potential (red line) analysis across the IMPs, as indicated in Fig. 5a. The potential difference shown in Fig. 5b, with a $\Delta\Psi$ of + 330 mV, indicates a cathodic behaviour of the IMPs relative to the Al matrix. Moreover, the height variation on a nanometric scale of the particle relative to the matrix causes discontinuity in the passive film, consequently reducing the corrosion resistance of the aluminium alloys.

Table 5 summarizes the average height and Volta potential of the IMPs present in the alloys under study. These results, obtained through the analysis of 15 IMPs in each alloy, reveal that the IMPs exhibit a positive Volta potential relative to the aluminium matrix. This indicates a distinct electrochemical behaviour compared to the Al matrix, underscoring variations in both the topographical and electrochemical characteristics of the IMPs across different aluminium alloys.

These results show distinct potentials of the IMPs compared to the Al matrix, highlighting variations in both,

Table 4 Average Cu/Fe and Cu/Mg ratios of the constituent intermetallic particles (IMPs) present in the Al alloys used in this study (wt.%). Results obtained through the analysis of 60 IMPs in each alloy

Aluminium Alloys	Relation among the elements present in IMPs		
	IMPs	Cu/Fe	Cu/Mg
AA2024-T3	Al-Cu-Mg	–	2.20 ± 0.9
	Al-Cu-Fe-Mn	3.1 ± 0.6	–
	Al-Cu-Fe-Mn-Si	1.5 ± 0.2	–
AA2198-T8	Al-Cu-Fe	2.8 ± 0.4	–
AA2198-T851		2.6 ± 0.2	–
AA7475-T761	Al-Cu-Fe (high copper containing)	2.16 ± 0.3	–
	Al-Cu-Fe (low copper containing)	0.4 ± 0.1	–

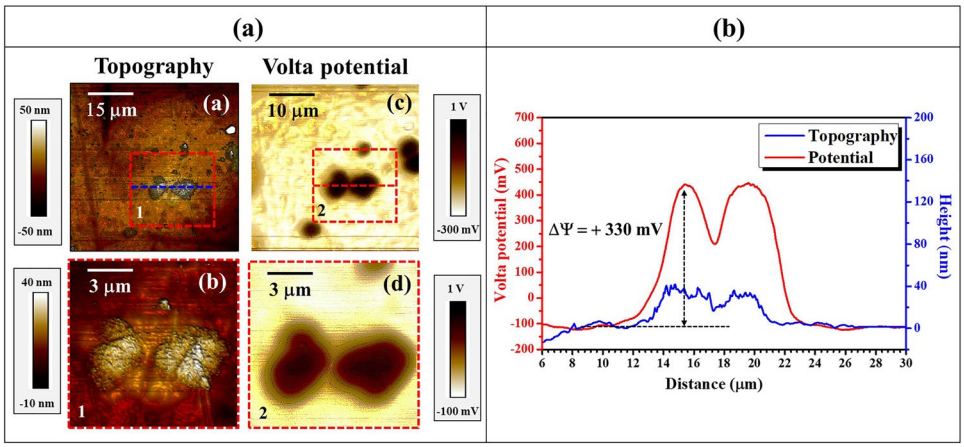

Fig. 5 **a** AFM images and **b** surface potential map of constituent intermetallic particles (IMPs) in the AA7475-T761 alloy, and **c** topography (line blue) and Volta potential line (line red) analysis across the IMPs indicated in (**a**)

Table 5 Average height and Volta potential of the constituent intermetallic particles (IMPs) present in the alloys under study. Results obtained through the analysis of 15 IMPs in each alloy

Aluminium alloys	Constituent intermetallic particles characteristics		
	Height (nm)	Volta potential (ΔΨ – mV)	Relative difference in Volta potential (%)
AA2024-T3	72.7 ± 21.3	+ 371.2 ± 77.8	–
AA2198-T8	34.5 ± 16.3	+ 403.1 ± 106.5	+ 8.6
AA2198-T851	55.2 ± 29.1	+ 312.4 ± 126.7	+ 6.6
AA7475-T761	48.1 ± 17.7	+ 368.5 ± 31.8	− 0.7

The relative difference is calculated using AA2024-T3 as the reference alloy.

topographical and electrochemical characteristics of the IMPs, across different aluminium alloys. The height of the IMPs in the AA2024-T3 alloy is the largest among the alloys studied (72.7 nm), which reflects its complex compositional nature and the prevalence of larger intermetallic phases. In contrast, the AA2198-T8 and AA7475-T761 alloys exhibit significantly lower heights, with reductions of 53% and 34%, respectively, relative to the AA2024-T3 alloy. The AA2198-T851 condition, with a height of 48.3 nm, shows intermediate behaviour, aligning closely with the AA7475-T761 alloy. These variations underline the impact of thermomechanical treatments and compositional differences on the size and distribution of intermetallic particles.

It is important to note that the measured height of the IMPs represents only the portion of the particles exposed above the polished surface of the aluminium alloy samples. The results reported here provide a two-dimensional view of the polished surface, as a significant part of the IMPs remains embedded within the aluminium matrix. This partial exposure limits the ability of topographical measurements to capture the full morphology and size of the particles. Such limitations may influence the measured Volta potential, as reported in the literature [48], where variations in the visible size or height of particles can alter the observed values. Since Volta potential is determined with atomic precision, larger or partially embedded particles may exhibit different electrochemical behaviours due to changes in their exposed surface area and interaction with the surrounding matrix.

In terms of electrochemical potential, the Volta potential values varied in a range from + 368.5 mV (AA7475-T761) to + 403.1 mV (AA2198-T8), with the AA2024-T3 alloy at + 371.2 mV and the AA2198-T851 at + 395.7 mV. The relative differences indicate that the AA2198 alloys (T8 and T851) exhibit slightly higher potentials compared to the AA2024-T3 alloy, with increases of 8.6% and 6.6%, respectively. These results suggest that the AA2198 alloys present a cathodic behaviour relative to the matrix, influenced by the presence of lithium and the specific thermomechanical treatments applied [49]. The AA7475-T761 alloy, on the other hand, shows the lowest potential difference (− 0.7%), highlighting its fairly compositional simplicity and uniformity of intermetallic phases.

The values reported in Table 5 are consistent with the SKPFM data reported for the AA2024 alloy in the works of Patrik Schmutz and Gerald S. Frankel [50], for the AA2198 alloy by Araujo et al. [17], and for the AA7475 alloy by Zhan et al. [51] in their studies of the AA7075 alloy.

Discussion

The differences observed among the studied alloys can be primarily attributed to their distinct chemical compositions and the specific thermomechanical treatments they have undergone. These factors play a crucial role in determining the size, distribution, and chemical nature of the IMPs in each alloy. A diagram to summarize the characteristics of these particles is provided in Fig. 6.

The AA2024-T3 (Al-Cu-Mg) alloy exhibited the highest density of IMPs per unit area, followed by the AA2198 (Al-Cu-Li) alloys in both T8 and T851 tempers, and finally the AA7475-T761 (Al-Zn-Mg) alloy, with the lowest IMPs density (Fig. 6a). The IMPs in the AA2024-T3 alloy also displayed greater morphological variability, indicating the

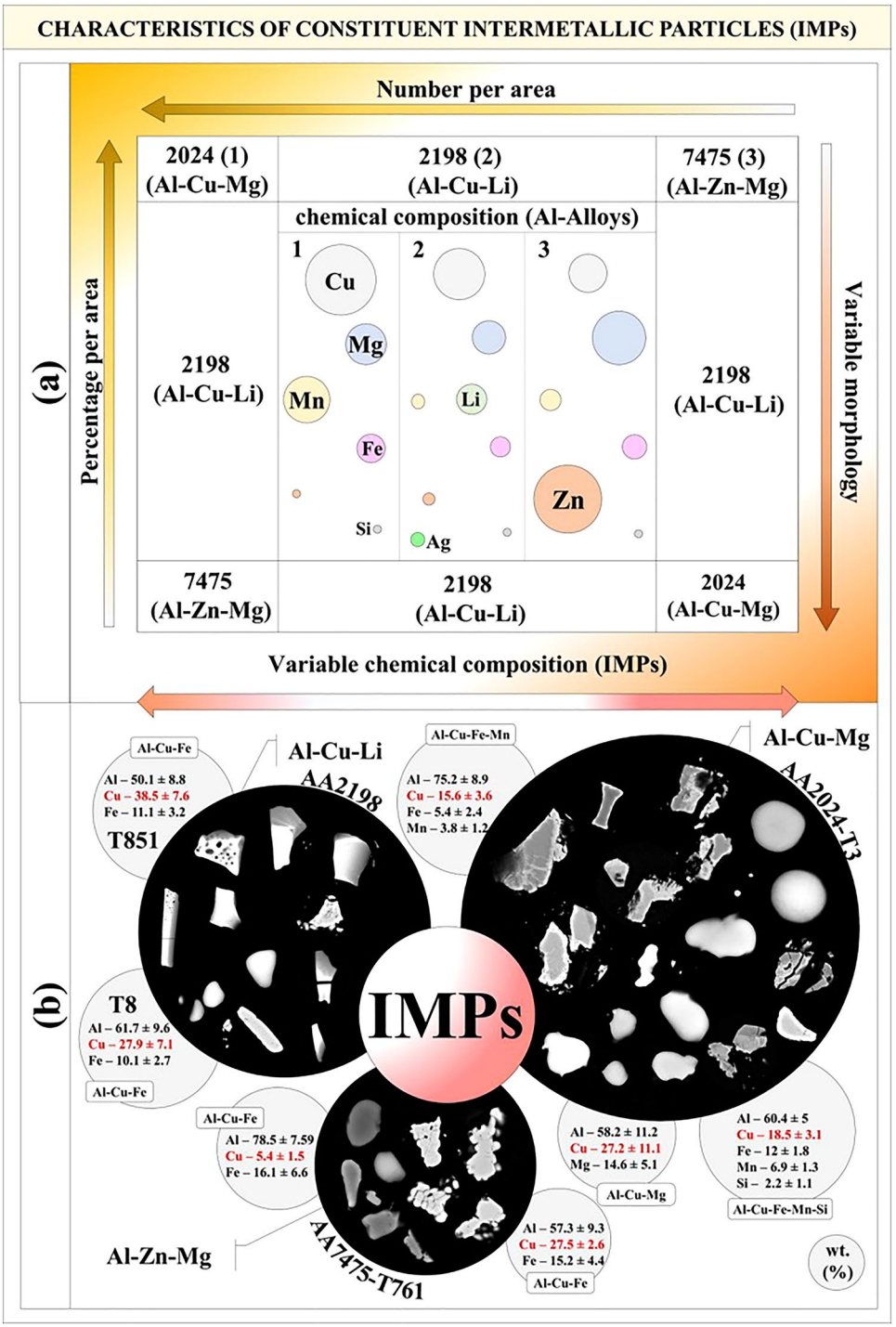

Fig. 6 **a** Diagram illustrating the characteristics of constituent intermetallic particles (IMPs) in the tested alloys. The coloured circles in the figure represent the relative amount of different alloying elements, with larger circles indicating higher concentrations; **b** the types of IMPs present in the alloys and their respective chemical compositions

significant influence of its complex chemical composition on particle formation.

As shown in Fig. 6b, the IMPs in the AA2024-T3 alloy exhibit a variety of shapes. The Al-Cu-Mg particles tend to be more spherical with smoother boundaries. On the other hand, the Al-Cu-Fe-Mn and Al-Cu-Fe-Mn-Si particles exhibit angular and irregular shapes. In the AA2198 alloy, the Al-Cu-Fe particles exhibit irregular shapes, often with faceted edges. In the AA7475-T761 alloy, high-copper-containing IMPs tended to have more angular and irregular shapes, while those with low-copper-containing ones generally had spherical morphologies with smooth boundaries.

The low solubility of Fe in all alloys, due to its low solubility in the Al matrix [40], explains its consistent identification in the IMPs across different compositions. In the AA2024-T3 alloy, three distinct types of IMPs were identified: Al-Cu-Mg, Al-Cu-Fe-Mn, and Al-Cu-Fe-Mn-Si. In contrast, the AA2198 alloy, characterized by its composition with Li, Cu, Mg, Fe, and Ag content, exhibited only Al-Cu-Fe IMPs. This suggests that the thermomechanical treatments applied to the AA2198 alloy did not significantly alter the composition of its IMPs. Studies [44] on the AA2099 alloy have shown that small variations in Li, Mn, and Zr content can substantially alter the composition of IMPs. However, such variations were not observed in the AA2198 alloy, highlighting the nuanced relationship between alloy composition and processing conditions.

The findings from the AA2198 alloy underscore the importance of precisely controlling alloying elements and thermomechanical treatments to achieve the desired microstructural characteristics. This suggests that alloy design strategies for the AA2198, and similar advanced aluminium alloys, must account for subtle compositional and processing variations to optimize the formation and distribution of intermetallic particles (IMPs). Previous studies, such as those conducted on the AA2099-T8 alloy [44], have identified the presence of Al–Fe–Mn–Cu multiphase particles, where phases with varying copper content are in distinct regions of the particle— high-copper-containing phases in the centre and low-copper-containing phases on the periphery. In contrast with these observations, the AA2198 alloy of the present study did not reveal such multiphase characteristics in its intermetallic particles, which were primarily composed of Al–Cu–Fe. The absence of these complex particle morphologies may be attributed to the specific thermomechanical treatments applied to the alloy, which seemingly did not significantly alter the composition of the IMPs [52]. Although the techniques used in this study (SEM and EDX) were sufficient to characterize the general composition and morphology of the particles, more advanced techniques, such as XRD/TEM, could provide additional insights into the crystal structure and phase distribution of the IMPs [7, 22, 45, 53]. These methods would be particularly useful in exploring potential multiphase characteristics that may have been overlooked due to the resolution limitations of the current analysis.

Nevertheless, the subtle relationship between alloy composition and processing conditions remains critical, as demonstrated by studies on the AA2099 alloy, where small variations in elements, such as Li, Mn, and Zr, can lead to substantial changes in the composition of the IMPs. Therefore, future research should focus on elucidating the specific mechanisms by which these factors influence IMPs evolution, with the aim of enhancing mechanical properties and corrosion resistance, particularly in aerospace applications.

For the AA7475-T761 alloy, two types of IMPs were observed, characterized by low and high copper containing. Despite containing Zn, Mg, Cu, and Fe, only Cu and Fe were identified in its IMPs, likely due to the high solubility of Zn and Mg in the Al matrix. The formation of low-copper-containing IMPs, as suggested by Ma and co-authors [44], must result from diffusion of Cu from high-copper-containing ones to the surrounding matrix during homogenization and subsequent thermomechanical processing. This underscores the significant impact of thermal treatment and processing conditions on IMPs formation.

The chemical composition and resulting microstructural characteristics of the AA7475-T761 alloy are critical to its superior resistance to localized corrosion. The lower copper content observed in certain IMPs likely reduces their cathodic activity relative to the aluminium matrix [54, 55]. This reduction in cathodic activity minimizes the tendency for trenching corrosion, a phenomenon where high-copper-containing IMPs, as observed in systems like AA2024-T3 [49, 54, 56, 57], act as strong cathodic sites, accelerating the anodic dissolution of the surrounding matrix. Moreover, the homogeneity of morphology and distribution of these low-copper-containing IMPs likely contribute to the improved corrosion resistance of the AA7475-T761 system in aggressive environments. These findings underscore the importance of tailoring particle composition through precise alloying and thermomechanical treatments to optimize corrosion resistance, particularly in aerospace applications where environmental durability is critical.

Low-copper-containing particles were found in the AA7475-T761 alloy but were absent in the other alloys studied, although they have been reported in the Al-Cu-Li AA2099 alloy. The differences in Zn, Mg, and Cu content between the AA7475-T761 and AA2099 alloys, along with the absence of Li in the former, suggest that specific processing conditions, or subtle compositional differences, play a critical role in IMP formation. The AA2198 alloy, differing from the AA2099 by having less Mn, more Ag, and more Cu, did not exhibit multiphase particles, indicating that the chemical composition of IMPs should not be generalized across alloy classes. This highlights the limitations

of relying solely on broad generalizations found in standard handbooks, which often lack the level of detail required to predict the nuanced effects of IMPs on corrosion resistance or anodization behaviour across different alloys. Comparative studies, like the present work, are essential to bridge this gap and provide a deeper understanding of these phenomena.

Considering these findings, it is clear that each aluminium alloy requires comprehensive investigation to fully understand the formation and evolution of IMPs. These studies must account for the complete manufacturing history, including precise chemical compositions and processing conditions. For instance, the differences observed in the AA2024-T3 alloy, which exhibited the highest density and greatest morphological variability of IMPs, highlight the need for alloy-specific studies. Previous studies, such as those reported in the literature on the AA2099 alloy [44, 58, 59], also indicate that small variations in alloying elements can significantly alter the composition of IMPs. These studies are crucial for developing optimized processing protocols that can effectively control the characteristics of IMPs, ultimately enhancing the mechanical property, corrosion resistance, and overall durability of high strength aluminium alloys.

Moreover, the distinct behaviours observed among different aluminium alloys, such as the AA2099 reported in the literature [44], and the AA2198 [17], the focus of this study, suggest that even subtle compositional and processing variations can substantially impact the formation and distribution of IMPs. This underscores the limitations of broad generalizations across alloy systems and reinforces the importance of conducting detailed, alloy-specific investigations. These studies will allow a deeper understanding of the microstructural factors influencing IMPs behaviours, which is essential for advancing alloy design and processing strategies. In particular, such research will be critical for aerospace applications, where improving the performance of aluminium alloys is critical to achieving superior mechanical properties and long-term reliability under demanding service conditions.

Conclusions

a) The AA2024-T3 alloy is characterized by at least three primary types of constituent intermetallic particles (IMPs): Al-Cu-Mg, Al-Cu-Fe-Mn, and Al-Cu-Fe-Mn-Si. In contrast, the AA2198 alloys of this study predominantly contain a single type of constituent particle, identified as Al-Cu-Fe. The AA7475-T761 alloy shows two types of IMPs with varying Cu contents, one of low copper containing and another of high copper containing.

b) The sizes of the IMPs vary significantly between the alloys of this study. The AA2024-T3 alloy exhibits the greatest variation, with particle sizes ranging from 1 µm to 22 µm, while the AA2198 alloys show particle sizes ranging from 1 µm to 14 µm. In the AA7475 alloy, the IMPs are significantly smaller, with sizes ranging from 1 µm to 12 µm.

c) The chemical composition of the IMPs shows significant variations, particularly in copper content. In the AA2024-T3 alloy, copper content ranges from 15.6 wt.% to 27.2 wt.%, depending on the type of IMP, while in the AA2198 alloys, the copper content is consistently high, ranging from 27.9 wt.% to 38.5 wt.%. In the AA7475 alloy, IMPs were observed with two types of copper content: high (around 27.5 wt.%)- and low (nearly 5.4 wt.%)-copper-content ones.

d) The techniques employed in this study, including SEM and EDX, provided valuable insights into the morphology, size, and composition of the IMPs. However, future studies employing advanced techniques, such as XRD/TEM, could reveal additional details about the crystalline structure and phase distribution of these particles, particularly in alloys like AA2198, where no multiphase characteristics were detected in the IMPs. Such studies would be crucial to further elucidate the impact of subtle compositional and processing variations on IMP formation and evolution.

Acknowledgements The authors gratefully acknowledge the financial support provided by FAPESP under grant numbers 2019/18388-1 and 2022/06935-0, awarded for the Ph.D. studies of João Victor de Sousa Araujo. Additionally, this work was supported by the EPSRC under grant EP/S004963/1.

Author Contributions João Victor de Sousa Araujo involved in investigation, visualization, writing—original draft. Isolda Costa took part in project administration, supervision, writing—review and editing. Xiaorong Zhou involved in supervision, writing—review and editing.

References

1. N. Eswara Prasad, T.R. Ramachandran, phase diagrams and phase reactions in Al–Li alloys, in *Aluminum-lithium alloys*. (Elsevier, 2014), pp.61–97 https://doi.org/10.1016/B978-0-12-401698-9.00003-3
2. F.W. Gayle, J.B. VanderSande, A.J. McAlister, The Al-Li (Aluminum-Lithium) system. Bull Alloy Phase Diagr. **5**(1), 19–20 (1984). https://doi.org/10.1007/BF02868711
3. D.G.E., A.A.A., N.A. Belov, Multicomponent phase diagrams. Elsevier, 2005. https://doi.org/10.1016/B978-0-08-044537-3.X5000-8
4. K.S. Prasad, N.E. Prasad, A.A. Gokhale, Microstructure and precipitate characteristics of aluminum-lithium alloys. Elsevier Inc., 2013. https://doi.org/10.1016/B978-0-12-401698-9.00004-5
5. N.E. Prasad, R.J.H. Wanhill, Aerospace Materials and Material Technology. Vol. 1 (2016).

6. P. Rambabu, N.E. Prasad, V.V. Kutumbarao, R.J.H. Wanhill, Aluminium alloys for aerospace applications. In: 29–52 (2017). https://doi.org/10.1007/978-981-10-2134-3_2
7. N. Birbilis, G.E. Zhou, High strength Al-alloys: microstructure, corrosion and principles of protection. Recent Trends Process Degrad Alum Alloys. (2011). https://doi.org/10.5772/18766
8. J.C. Grosskreutz, Mechanisms of metal fatigue part II. Phys. Status Solidi B. **47**, 359–368 (1971)
9. G.E. Thompson, H. Habazaki, K. Shimizu, M. Sakairi, G.C. Wood, Anodizing of aluminium alloys. Aircr. Eng. Aerosp. Technol. **71**, 228–238 (1999)
10. Y. Ma, H. Wu, X. Zhou, K. Li, Y. Liao, Z. Liang, L. Liu, Corrosion behavior of anodized Al-Cu-Li alloy: the role of intermetallic particle-introduced film defects. Corros. Sci. **158**, 108110 (2019). https://doi.org/10.1016/j.corsci.2019.108110
11. H. Wu, Y. Ma, W. Huang, X. Zhou, K. Li, Y. Liao, Z. Wang, Z. Liang, L. Liu, Effect of iron-containing intermetallic particles on film structure and corrosion resistance of anodized AA2099 alloy. J. Electrochem. Soc. **165**, C573–C581 (2018). https://doi.org/10.1149/2.1361809jes
12. Y. Ma, X. Zhou, J. Wang, G.E. Thompson, W. Huang, J.O. Nilsson, M. Gustavsson, A. Crispin, Discoloration of anodized AA6063 aluminum alloy. J. Electrochem. Soc. **161**, C119–C130 (2014). https://doi.org/10.1149/2.065406jes
13. A.E. Boag, A.M. Hughes, T.H. Glenn, D. Muster, McCulloch, corrosion of AA2024-T3 Part I: localised corrosion of isolated IM particles. Corros. Sci. **53**, 17–26 (2011). https://doi.org/10.1016/j.corsci.2010.09.009
14. A.M. Glenn, T.H. Muster, C. Luo, X. Zhou, G.E. Thompson, A. Boag, A.E. Hughes, Corrosion of AA2024-T3 part III: propagation. Corros. Sci. **53**, 40–50 (2011). https://doi.org/10.1016/j.corsci.2010.09.035
15. A.E. Hughes, A. Boag, A.M. Glenn, D. McCulloch, T.H. Muster, C. Ryan, C. Luo, X. Zhou, G.E. Thompson, Corrosion of AA2024-T3 part II: co-operative corrosion. Corros. Sci. **53**, 27–39 (2011). https://doi.org/10.1016/j.corsci.2010.09.030
16. J.V.S. de Araujo, R.M.P. da Silva, B.V.G. de Viveiros, R.E. Klumpp, I. Costa, Estudo do comportamento eletroquímico de uma liga Al-Cu-Li. Matéria (Rio J.). **29**, e20240002 (2024). https://doi.org/10.1590/1517-7076-rmat-2023-0328
17. J.V. de Sousa Araujo, A.F. Santos Bugarin, U. Donatus, C.S.C. Machado, F.M. Queiroz, M. Terada, A. Astarita, I. Costa, Thermomechanical treatment and corrosion resistance correlation in the AA2198 Al–Cu–Li alloy. Corros. Eng. Sci. Technol. **54**, 575–586 (2019). https://doi.org/10.1080/1478422X.2019.1637077
18. R. Grilli, M.A. Baker, J.E. Castle, B. Dunn, J.F. Watts, Localized corrosion of a 2219 aluminium alloy exposed to a 3.5% NaCl solution. Corros Sci. **52**(9), 2855–2866 (2010). https://doi.org/10.1016/j.corsci.2010.04.035
19. W. Zhang, G. Frankel, Localized corrosion growth kinetics in AA2024 alloys. J. Electrochem. Soc. **149**, B1–B11 (2002). https://doi.org/10.1149/1.1513984
20. Y. Zhu, K. Sun, G.S. Frankel, Intermetallic phases in aluminum alloys and their roles in localized corrosion. J. Electrochem. Soc. **165**, C807–C820 (2018). https://doi.org/10.1149/2.0931811jes
21. Y. Ma, X. Zhou, W. Huang, G.E. Thompson, X. Zhang, C. Luo, Z. Sun, Localized corrosion in AA2099-T83 aluminum-lithium alloy: the role of intermetallic particles. Mater. Chem. Phys. **161**, 201–210 (2015). https://doi.org/10.1016/j.matchemphys.2015.05.037
22. N. Birbilis, R.G. Buchheit, Electrochemical characteristics of intermetallic phases in aluminum alloys. J. Electrochem. Soc. **152**, B140–B151 (2005). https://doi.org/10.1149/1.1869984
23. F.M. Queiroz, H.G. De Melo, I. Costa, Effect of intermetallics on the corrosion of Al 2024–T3 alloy in solutions with different chloride concentrations. Mater. Sci. Forum. **587–588**, 415–419 (2008). https://doi.org/10.4028/www.scientific.net/MSF.587-588.415
24. S.P. Luo, X. Albu, Z. Zhou, X. Sun, Z. Zhang, G.E. Tang, Thompson, Continuous and discontinuous localized corrosion of a 2xxx aluminium-copper-lithium alloy in sodium chloride solution. J. Alloys Compd. **658**, 61–70 (2016). https://doi.org/10.1016/j.jallcom.2015.10.185
25. G.S. Frankel, T. Li, J.R. Scully, Perspective—localized corrosion: passive film breakdown vs pit growth stability. J. Electrochem. Soc. **164**, C180–C181 (2017). https://doi.org/10.1149/2.1381704jes
26. J.V. de Sousa Araujo, M. Milagre, I. Costa, A historical, statistical and electrochemical approach on the effect of microstructure in the anodizing of Al alloys: a review. Crit Rev Solid State Mater Sci. **49**(4), 521–81 (2024)
27. J.V. de Sousa Araujo, M.X. Milagre, R.E. Klumpp, V.H. Ayusso, U. Donatus, I. Costa, TSA anodising voltage effects on the near-surface coarse intermetallic particles in the AA2024-T3 and AA2198-T8 alloys. Corros. Eng. Sci. Technol. **57**, 380–396 (2022). https://doi.org/10.1080/1478422X.2022.2071666
28. J. Araujo, R. Pereira, R. Klumpp, I. Costa, O processo de anodização do alumínio e suas ligas: Uma abordagem histórica e eletroquímica. Quim. Nova. **44**, 896–908 (2021). https://doi.org/10.21577/0100-4042.20170748
29. Y. Ma, X. Zhou, G.E. Thompson, M. Curioni, X. Zhong, E. Koroleva, P. Skeldon, P. Thomson, M. Fowles, Discontinuities in the porous anodic film formed on AA2099-T8 aluminium alloy. Corros. Sci. **53**, 4141–4151 (2011). https://doi.org/10.1016/j.corsci.2011.08.023
30. R. Boag, T. Taylor, Muster, Stable pit formation on AA2024-T3 in a NaCl environment. Corros. Sci. **52**, 90–103 (2010). https://doi.org/10.1016/j.corsci.2009.08.043
31. L.E.M. Palomino, I.V. Aoki, H.G. de Melo, Microstructural and electrochemical characterization of Ce conversion layers formed on Al alloy 2024–T3 covered with Cu-rich smut. Electrochim. Acta. **51**, 5943–5953 (2006). https://doi.org/10.1016/j.electacta.2006.03.036
32. U. Tiringer, J. Kovač, I. Milošev, Effects of mechanical and chemical pre-treatments on the morphology and composition of surfaces of aluminium alloys 7075–T6 and 2024–T3. Corros. Sci. **119**, 46–59 (2017). https://doi.org/10.1016/j.corsci.2017.02.018
33. H.C. Shih, N.J. Ho, J.C. Huang, Precipitation behaviors in Al-Cu-Mg and 2024 aluminum alloys. Metall. Mater. Trans. A. **27**, 2479–2494 (1996). https://doi.org/10.1007/BF02652342
34. J. Corral, E.A. Trillo, Y. Li, L.E. Murr, Corrosion of friction-stir welded aluminum alloys 2024 and 2195. J. Mater. Sci. Lett. **19**, 2117–2122 (2000). https://doi.org/10.1023/A:1026710422951
35. I.V. Gordovskaya, M. Curioni, T. Hashimoto, J. Walton, G.E. Thompson, P. Skeldon, Characterization of 2024–T3 aluminum alloy after rare earth desmutting. J. Electrochem. Soc. **163**, C253–C259 (2016). https://doi.org/10.1149/2.0201606jes
36. J.A.C. Miramontes, B.S. Martínez-Aparicio, F.J. Olguín-Coca, L.D.L. León, Francisco Estupiñan-Lopez, C.G. Tiburcio, P. Zambrano, F. Almeraya-Calderón, Corrosion resistance of alloy 2024 anodized on sulfuric-citric acid. ECS Trans. **94**(1), 73–80 (2019). https://doi.org/10.1149/09401.0073ecst
37. R.P.W.C.M. Liao, J.M. Olive, M. Gao, In-situ monitoring of pitting corrosion in aluminium alloy 2024. Corros. Sci. **54**, 451–458 (1998)
38. J. Larignon, E. Alexis, L. Andrieu, G. Lacroix, C. Odemer, Blanc, Combined Kelvin probe force microscopy and secondary ion mass spectrometry for hydrogen detection in corroded 2024 aluminium alloy. Electrochim. Acta. **110**, 484–490 (2013). https://doi.org/10.1016/j.electacta.2013.02.063

39. D. Georgoulis, C.M. Charalampidou, N. Siskou, N.D. Alexopoulos, S.K. Kourkoulis, Corrosion behaviour of AA2198–T8 and AA2024-T3 alloy in 3.5% aqueous solution. Proce Struct Integr. **28**, 2297–2303 (2020). https://doi.org/10.1016/j.prostr.2020.11.076
40. G.E. Totten, D.S. MacKenzie (eds.), Handbook of Aluminum. CRC Press (2003). https://doi.org/10.1201/9780203912607
41. American Society for Materials, ASM Handbook: Properties and selection: nonferrous alloys and special-purpose materials. ASM International (2001). https://doi.org/10.31399/asm.hb.v02.a0001204
42. J.C. Benedyk, International temper designation systems for wrought aluminium alloys: Part II–thermally treated (T Temper) aluminium alloys. Light Metal Age. **68**, 34–36 (2010)
43. J.R. Davis, Aluminum and Aluminum Alloys. ASM International, Materials Park, 784 (1993).
44. Y. Ma, X. Zhou, G.E. Thompson, T. Hashimoto, P. Thomson, M. Fowles, Distribution of intermetallics in an AA2099-T8 aluminium alloy extrusion. Mater. Chem. Phys. **126**, 46–53 (2011). https://doi.org/10.1016/j.matchemphys.2010.12.014
45. C.M. MacRae, A.E. Hughes, J.S. Laird, A.M. Glenn, N.C. Wilson, A. Torpy, M.A. Gibson, X. Zhou, N. Birbilis, G.E. Thompson, An examination of the composition and microstructure of coarse intermetallic particles in AA2099-T8, including Li detection. Microsc. Microanal. **24**, 17–27 (2018). https://doi.org/10.1017/S1431927618000454
46. F.M. Queiroz, M. Magnani, I. Costa, H.G. de Melo, Investigation of the corrosion behaviour of AA 2024–T3 in low concentrated chloride media. Corros. Sci. **50**, 2646–2657 (2008). https://doi.org/10.1016/j.corsci.2008.06.041
47. G.S. Chen, M. Gao, R.P. Wei, Microconstituent-induced pitting corrosion in aluminum alloy 2024–T3. Corrosion. **52**, 8–15 (1996). https://doi.org/10.5006/1.3292099
48. C. Örnek, J. Leygraf, Pan, On the Volta potential measured by SKPFM – Fundamental and practical aspects with relevance to corrosion science. Corros. Eng. Sci. Technol. **54**, 185–198 (2019). https://doi.org/10.1080/1478422X.2019.1583436
49. M.X. Milagre, J.V. de S. Araujo, M. Pereira, U. Donatus, C.S.C. Machado, I. Costa, Comparison of the corrosion resistance of AA2024 and AA2098 alloys in different solutions. Proc. Eur. Corrosion Congress (2018).
50. P. Schmutz, Characterization of AA2024-T3 by scanning Kelvin probe force microscopy. J. Electrochem. Soc. **145**, 2285–2295 (2006). https://doi.org/10.1149/1.1838633
51. C. Zhang, J.O. Örnek, J. Nilsson, Pan, Anodisation of aluminium alloy AA7075—Influence of intermetallic particles on anodic oxide growth. Corros. Sci. **164**, 108319 (2020). https://doi.org/10.1016/j.corsci.2019.108319
52. Y. Lv, T. Hashimoto, X. Zhou, X. Zhang, Influence of thermomechanical treatment on the corrosion behaviour of 2A97 Al-Cu-Li alloy. Corros. Commun. **15**, 13–23 (2024). https://doi.org/10.1016/j.corcom.2023.10.003
53. D.K. Xu, N. Birbilis, P.A. Rometsch, The effect of pre-ageing temperature and retrogression heating rate on the strength and corrosion behaviour of AA7150. Corros. Sci. **54**, 17–25 (2012). https://doi.org/10.1016/j.corsci.2011.08.042
54. U. Donatus, M.O. Bodunrin, A. Olayinka, M.X. Milagre, O.R. Oloyede, A. Sunday, I. Costa, A comparison between new generation Al-Cu-Li and conventional alloys. Adv. Al Compos. Alloys. **1**, 159–171 (2021)
55. J.V. Araujo, M.X. Milagre, A.D. Gabbardo, R.E. Klumpp, I. Costa, (Digital Presentation) The effect of tartaric-sulfuric acid (TSA) anodizing on the corrosion resistance of the AA7475-T761. ECS Meet Abstr. (2022). https://doi.org/10.1149/MA2022-02142475mtgabs
56. R.M.P. Silva, M.X. Milagre, L.A. Oliveira, U. Donatus, R.A. Antunes, I. Costa, The local electrochemical behavior of the AA2098-T351 and surface preparation effects investigated by scanning electrochemical microscopy. Surf. Interface Anal. **51**, 982–992 (2019). https://doi.org/10.1002/sia.6682
57. M.X. Milagre, U. Donatus, C.S.C. Machado, V.S. João, R.M. Araujo, P. da Silva, V.G. Bárbara, A. de Viveiros, I.C. Astarita, Comparison of the corrosion resistance of an Al–Cu alloy and an Al–Cu–Li alloy. Corr Eng Sci Technol. **54**(5), 402–412 (2019). https://doi.org/10.1080/1478422X.2019.1605472
58. M. Romios, R. Tiraschi, C. Parrish, H.W. Babel, J.R. Ogren, O.S. Es-Said, Design of multistep aging treatments of 2099 (C458) Al-Li alloy. J. Mater. Eng. Perform. **14**, 641–646 (2005). https://doi.org/10.1361/105994905X64594
59. Y. Lin, Z.Q. Zheng, S.C. Li, Effect of solution treatment on microstructures and mechanical properties of 2099 Al-Li alloy. Arch. Civ. Mech. Eng. **14**, 61–71 (2014). https://doi.org/10.1016/j.acme.2013.07.005